Two-dimensional flow of foam around an obstacle: Force measurements

Benjamin Dollet,[1] Florence Elias,[2] Catherine Quilliet,[1] Christophe Raufaste,[1] Miguel Aubouy,[3] and François Graner[1,*]

[1]*Laboratoire de Spectrométrie Physique, BP 87, 38402 Saint-Martin-d'Hères Cedex, France*

[2]*Laboratoire des Milieux Désordonnés et Hétérogènes, case 78, 4 place Jussieu, 75252 Paris Cedex 05, France*

[3]*SI3M, DRFMC, CEA, 38054 Grenoble Cedex 9, France*

A Stokes experiment for foams is proposed. It consists of a two-dimensional flow of a foam, confined between a water subphase and a top plate, around a fixed circular obstacle. We present systematic measurements of the drag exerted by the flowing foam on the obstacle versus various separately controlled parameters: flow rate, bubble volume, bulk viscosity, obstacle size, shape, and boundary conditions. We separate the drag into two contributions: an elastic one (yield drag) at vanishing flow rate and a fluid one (viscous coefficient) increasing with flow rate. We quantify the influence of each control parameter on the drag. The results exhibit in particular a power-law dependence of the drag as a function of the bulk viscosity and the flow rate with two different exponents. Moreover, we show that the drag decreases with bubble size and increases proportionally to the obstacle size. We quantify the effect of shape through a dimensional drag coefficient, and we show that the effect of boundary conditions is small.

PACS number(s): 82.70.Rr, 83.80.Iz, 47.50.+d, 47.60.+i

I. INTRODUCTION

Liquid foams, like colloids, emulsions, polymers, or surfactant solutions, are characterized by a complex mechanical behavior. These systems, known as soft complex systems, are multiphasic materials. Their constitutive entities are in interaction, generating internal structures, which cause diverse rheological behavior [1]. Liquid foams are convenient model experimental systems for studying the interplay between structure and rheology, since their internal structure can be easily visualised and manipulated.

Liquid foams are made of polyhedral gas bubbles separated by thin liquid boundaries forming a connected network. The liquid phase occupies a small fraction of the volume of the foam (a few percent for a dry foam). The deformations and motions of liquid foams are very diverse: foams are elastic, plastic, or viscous depending on the applied strain and strain rate [2]. This behavior has been shown in rheological experiments performed on three-dimensional (3D) foams [3–6]; models have been built to account for this diversity of rheological behavior [7–11]. However, the visualization of the foam structure is technically difficult in 3D [12,13], although progresses have been made recently [14]. Moreover, the drainage of the liquid phase due to gravity may occur in 3D, making the fluid fraction and therefore the rheological moduli of the foam, as well as bubble size (through coarsening), inhomogeneous [15].

For all these reasons, the mechanics of foams has been studied in two dimensions, where direct visualization of the structure is easier and no gravity-driven drainage occurs if the system is horizontal. The system is then either a true 2D system (unlike bubble raft [18,19]), like a Langmuir foam [16,17], or a quasi-2D system constituted by a monolayer of bubbles, either confined between two horizontal transparent plates (Hele-Shaw cells [20–22]: incompressible foams; see below) or between the surface of the solution and an upper horizontal transparent plate [20,23] (compressible foams; see below). The deformation and motion of individual cells have been forced and studied in different flow geometries: simple shear [18], flow in a constriction or around an obstacle [22], and Couette flow [19,21]. Some authors have been particularly interested in the dynamics of bubble rearrangements during the flow: the spatial distribution of the rearrangements [18,21], the stress relaxation associated with the rearrangements [19], the deformation profile [24], and the averaged velocity [21,22]. However, no mechanical measurement has been performed in those last studies.

In this paper, we study the mechanics of a foam flowing in relative displacement with respect to an obstacle, at a constant velocity. In a Newtonian liquid at low Reynolds number, the force would vary linearly with the foam-obstacle relative velocity, the proportionality factor being linked to the liquid viscosity and the size of the obstacle. This experiment gives information on the effective viscosity of a flowing foam. Such a Stokes experiment was first performed in a 3D coarsening foam by Cox *et al.* [25]. Here, we measure the force exerted by the quasi-2D foam on the obstacle, as a function of the flow velocity, in a 2D geometry. A similar experiment has been performed recently to investigate the elastic regime of a 2D foam and measure the foam shear modulus [17]. In the experiments presented here, the foam flows permanently around the obstacle, and the stationary regime is investigated. The system used is a monolayer of soap bubbles confined between the surface of the solution and a horizontal plate. This allows measuring accurately the forces exerted on the obstacle (Sec. II B) and varying easily the foam internal parameters such as the viscosity of the solution, the bubble size, and the geometry of the obstacle.

The article is organized as follows. The experimental materials and methods are presented in Sec. II, and the results are shown in Sec. III. These results are discussed in Sec. IV, and conclusions are exposed in Sec. V.

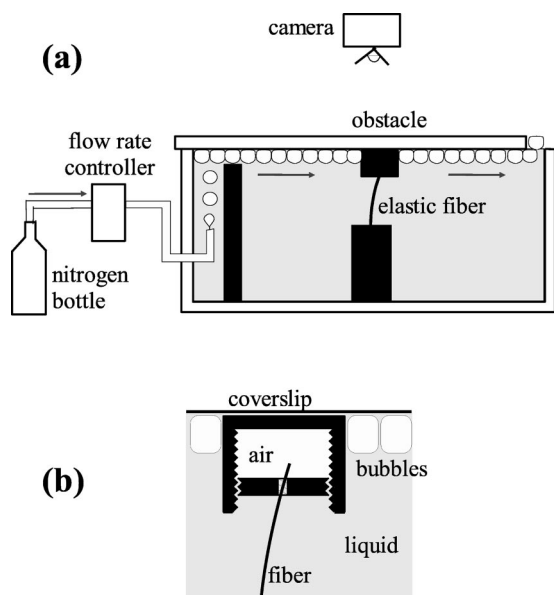*Electronic address: graner@spectro.ujf-grenoble.fr

(a)

(b)

FIG. 1. (a) Experimental setup. The arrows indicate the flow of gas and foam. (b) Detailed sketch of the obstacle.

FIG. 2. Photo of foam flowing from left to right around a circular obstacle of diameter 30 mm. The bubble size is 16.0 mm^2 (note the monodispersity of the foam), and the flow rate is 174 ml min^{-1}. The walls of the channel (width 10 cm) are visible at the top and bottom of the picture. The stretching and shearing of bubbles due to the presence of the obstacle is clearly visible around the obstacle. The surface of the observed field is 15.4×10.2 cm^2, and 1 pixel side equals 0.20 mm. Films are available at http://www-lsp/link/mousses-films.htm at low (17 ml/min), moderate (112 ml/min), and high (515 ml/min) flow rates for this obstacle and bubble area.

II. MATERIALS AND METHODS

A. Foam production

The experimental setup is presented in Fig. 1(a). The experiments are performed in a glass channel of 110 cm length, 10 cm width, and 10 cm depth. The soap solution is a solution of commercial dish-washing fluid (1% in volume) in purified water, with added glycerol when the viscosity needs to be varied (Sec. III A). We have measured the surface tension of two solutions with an apparatus based on the oscillating bubble method (IT Concept): $\gamma = 26.1 \pm 0.1$ mN m^{-1} for a solution with glycerol, and $\gamma = 24.24 \pm 0.04$ mN m^{-1} for a solution with 50% glycerol in mass. At the beginning of each experiment, the channel is filled with the solution, with a gap of thickness 3.50 ± 0.05 mm between the liquid surface and the coverslip. The foam is produced by blowing bubbles of nitrogen in the solution, at one end of the channel, in a chamber bounded by a barrier which allows a single monolayer of bubbles to form. The continuous gas flow makes the foam flow along the channel, between the surface of the solution and the coverslip, until it reaches the open end of the channel, where bubbles pop in contact with the atmosphere. Leaks are carefully avoided, so that the total amount of liquid in the channel is constant during an experiment and for each experiment. A typical image of the flowing foam observed from above is displayed in Fig. 2.

B. Obstacle and force measurements

The obstacle stands in the middle of the channel. It is a buoyant mobile plastic cylinder connected to a fixed base by a soft glass fiber. The bottom extremity of the fiber is rigidly fixed. Its top extremity simply passes through a hole drilled in the bottom of the cylinder [Fig. 1(b)]. Therefore, the fiber can slide inside the horizontally moving cylinder, without applying any undesirable vertical force. Moreover, the fiber
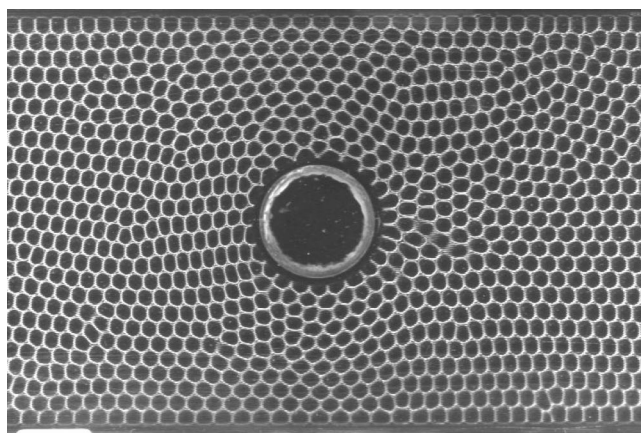
is lubricated by the liquid, which avoids solid friction against the cylinder.

The horizontal force F exerted by the foam on the obstacle tends to pull it streamwise; it is balanced by the horizontal drawback force F_d from the elastic fiber, which deflection is designed by X. The calculation of this force is classical in the theory of elasticity [26]; since the deflection of the fiber is too large to use linear Hooke's law, we use the following one:

$$F_d = -\frac{\pi E D^4}{64 L^2}\left[3\frac{X}{L} - \frac{81}{35}\left(\frac{X}{L}\right)^3 + \frac{29646}{13475}\left(\frac{X}{L}\right)^5 + O\left(\frac{X}{L}\right)^7 \right],$$

(1)

where $D = 240$ μm is the fiber diameter, L its vertical length, and E its shear modulus. This expansion gives a precision of 0.3% over the force. The derivation of formula (1) is detailed in the Appendix. The fiber has been calibrated by measuring its deflection under its own weight, giving the value of the parameter $ED^4 = (2.21 \pm 0.02) \times 10^{-4}$ Pa m^4. This value is compatible with typical values of the Young modulus of glass: $6-7 \times 10^{10}$ Pa. We use two different fibers of vertical lengths: $L = 34.8 \pm 0.1$ mm and $L = 42.4 \pm 0.1$ mm, depending on the magnitude of the force to measure. We have checked that for given experimental conditions, the same force measured with both fibers yields the same result (data not shown). The displacement is measured by tracking the position of the obstacle with a charge-coupled-device (CCD) camera placed above the channel: the actual position of the obstacle is given by the coordinates of its center, obtained by image analysis. The position of the center of the obstacle is known with a precision of 0.02 mm, much lower than the

typical displacement (0.5–1 cm). When the obstacle has reached a stationary position under flow, the drawback force exactly compensates the force exerted by the foam, which is then directly deduced from the measured displacement.

The obstacle is in contact with the coverslip. This is necessary for the foam to flow around the obstacle and not above it, but this may induce friction. Nevertheless, in the setup presented here, the obstacle is in contact with a single plate; this reduces the friction in comparison with an experiment performed in a Hele-Shaw cell, where the foam is confined between two plates. Furthermore, the obstacle has an enclosed cavity closed by a watertight screw [Fig. 1(b)], which enables one to tune its buoyancy such that the contact force with the top plate is minimal. In the presence of the foam, the obstacle is in contact with the top plate through a capillary bridge, avoiding solid friction. We check for each experiment that the obstacle is not stuck: its position fluctuates under the slight flow heterogeneities, and results presented below average the position of the obstacle over 50 successive images with an interval of two seconds. Viscous friction between the obstacle and the coverslip cannot be eliminated, but it only influences transients, which are not considered in this paper: each measurement is performed in a stationary regime. Reversibility and reproducibility tests give an upper bound for the force measurement errors: 0.2 mN, to be compared to the typical forces, of the order of 5 mN.

As shown by Fig. 1(b), a part of the obstacle is immersed in the subphase, which may be drawn by the flowing foam. This flowing subphase exerts an additional force on the obstacle, which is negligible as shown by the following evaluation. The total height of the obstacle is 23 mm, so the immersed height is $h \simeq 19.5$ mm because the foam thickness remains close to the initial thickness of 3.5 mm between the solution and the coverslip. Therefore, a generous upper bound of the drag exerted by the subphase would be obtained by assuming that the subphase flows at the same velocity V that the foam. The diameter of the obstacle being $2R = 30$ mm and the width of the channel $2H = 10$ cm, the drag exerted by the flowing subphase of dynamic viscosity η would equal [27]

$$F_{\text{subphase}} \simeq \frac{4\pi\eta hV}{\ln H/R - 0.91}.$$ (2)

By taking the highest foam velocity reached in the experiments, $V = 3$ cm s^{-1}, and the highest dynamic viscosity used, $\eta = 9 \times 10^{-3}$ Pa s, the upper bound of the force would be then evaluated to $F_{\text{subphase}} = 0.2$ mN, which is comparable to the other sources of error and much lower than the typical forces exerted by the foam on the obstacle.

C. Control parameters

A first control parameter is the nitrogen flow rate Q, which is adjusted using an electronic controller (Brooks Instrument B.V.) driven by a homemade software. The range of available flow rate runs on more than three decades, from 1 to 2000 ml min^{-1}, with a precision of 0.1 ml min^{-1}. Another control parameter is the bubble volume. It is indirectly determined by measuring the surface density of bubbles

against the coverslip thanks to image analysis, using NIH Image software. Since the mean foam thickness is fixed by the total amount of liquid in the channel, which is carefully kept constant, there is a unique relation between the bubble volume and the mean surface density. Instead of this surface density, we will refer throughout this paper to its inverse, which we shall call the mean bubble area. This parameter slightly differs from the bubble area one can measure directly on an image, because it includes the water contained in the films and plateau borders surrounding bubbles. In our setup, contrary to Hele-Shaw cells, the depth of the bubbles is free to adjust to pressure variations; this entails an effective compressibility of the flow and local variations of bubble area near the obstacle, as we shall see later (Sec. IV C). The surface density is measured at the left extremity of the observed field, where the influence of the obstacle is not significant (Fig. 12).

For a given injector, the bubble volume increases with the gas flow rate. To control these two parameters separately, we blow the gas through one to six tubes (or needles) of same diameter simultaneously, keeping constant the flow rate per tube, hence the bubble volume. Furthermore, the diameter of these injectors can be varied, which changes the flow rate per tube for the same bubble area; hence, for a given bubble volume, typically ten different values of flow rate are available (from 5 to 13 in the following data), with greatest flow rate at least 20 times greater than the lowest one. In this paper, we always produce monodisperse foams: the bubble area disorder, measured as the ratio of the standard deviation with the mean value of the bubble area distribution, is lower than 5%. Six different bubble areas were used: 12.1, 16.0, 20.0, 25.7, 31.7, and 39.3 mm^2, chosen with a relative precision of 3%. The study of smaller bubbles would be problematic, since a transition from bubble monolayer to multilayer occurs at low bubble width/height ratio [28]. At the other extremity, we cannot make a monodisperse foam with larger bubbles.

Another tunable parameter is the viscosity of the solution, which we will call bulk viscosity throughout the text. We control it by adding glycerol to the initial soap solution. We have used five different solutions, with 0%, 20%, 30%, 40%, and 50% glycerol in mass. The respective kinematic viscosities ν, measured with a capillary viscometer (Schott-Geräte) at room temperature, are equal to 1.06, 1.6, 2.3, 3.8, and 9.3 mm^2 s^{-1}. The variation of viscosity due to the variation of room temperature is lower than 4%.

Different obstacles have been used (Fig. 3). To change the obstacle, additional profiles are fixed on the previously described cylinder; for each obstacle, the apparent density is tuned to avoid solid friction (Sec. II B). Two different cylinders of diameter 30.0 [Fig. 3(a)] and 48.0 mm [Fig. 3(b)] are used to study the influence of size. Boundary conditions on the obstacle are investigated using a cogwheel of diameter 43.5 mm, with circular cogs of diameter 4.0 mm [Fig. 3(c)]: whereas flowing foam slips along any smooth obstacle, the cogs trap the first layer of bubbles surrounding the cogwheel. A square obstacle, of side 33.9 mm [Fig. 3(d)], is used to study orientation effects. Furthermore, we made an airfoil profile [Fig. 3(e)] to study possible streamlining. It is a standard NACA 0025 profile, which means that it is not cam-
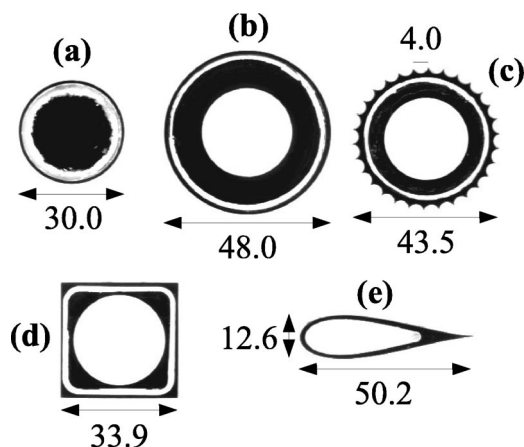
FIG. 3. Top views of the five obstacles, with dimensions in millimeters.

bered and that its maximal thickness (12.6 mm) equals 25% of its total length (50.2 mm). This profile was homemade using a numerical milling machine (Deckel-Maho); its mathematical expression, parametrized by the angle t running from $-\pi$ to π, writes $x(t)=25.1\cos t$, $y(t)=4.83(1+\cos t)\sin t$, where the lengths are expressed in millimeters.

III. RESULTS

A. Influence of the bulk viscosity

We study the variation of the drag versus the flow rate and the bulk viscosity, for the five different viscosities indicated in Sec. II C. All these measurements are performed at a fixed bubble area of 20 mm², and we use a circular obstacle of diameter 30 mm (Fig. 3).

We observe two general features (Fig. 4), independent of the value of the bulk viscosity: the drag does not tend to zero at vanishing flow rate, and it increases with flow rate. The first observation is a signature of the solidlike properties of the foam. The second feature is related to the fluidlike prop-
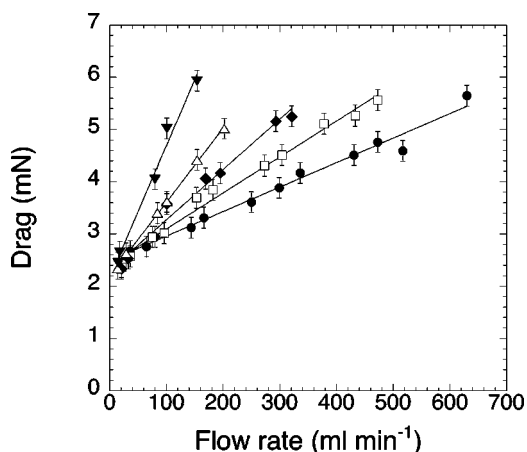

FIG. 4. Drag vs flow rate, for bulk viscosity equal to 1.06 (●), 1.6 (□), 2.3 (◆), 3.8 (△), and 9.3 mm² s⁻¹ (▼). The straight lines are linear fits of the data. The bubble area is 20 mm² and the obstacle is a circle of diameter 30 mm.
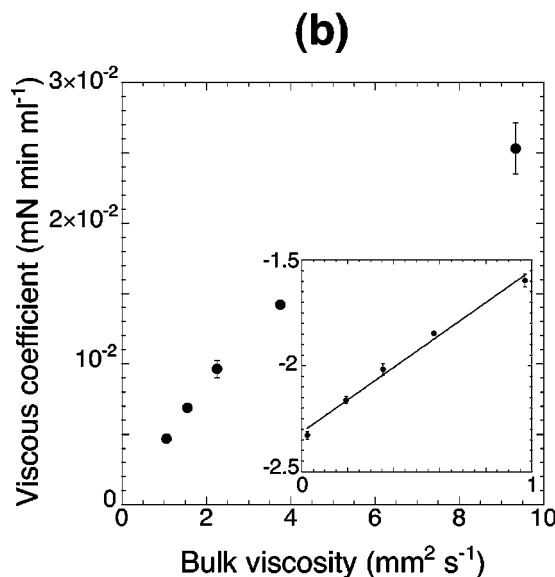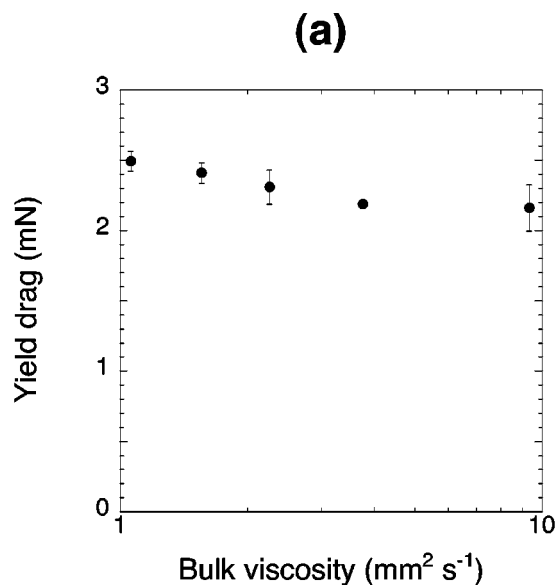

FIG. 5. Results from fits to Fig. 4. (a) Yield drag vs the bulk viscosity (semilogarithmic scale) and (b) viscous coefficient vs the bulk viscosity (linear scale). Inset: log-log plot. All error bars indicate the incertitude on the fit parameter arising from statistical dispersion of the data. The straight line is the linear fit: its slope is 0.77 ± 0.05.

erties of the foam. The data are well fitted by a linear law (Fig. 5)

$$F = F_0 + mQ. \qquad (3)$$

We call F_0 the yield drag, as a reference to the yield properties of the foam, and the slope m the viscous coefficient, since we can dimensionally deduce from m an effective 3D viscosity μ for the foam: $\mu \approx mS/R$, where S is the cross section of the foam and R is the typical size of the obstacle. Yield drag versus bulk viscosity is plotted in Fig. 5(a) and viscous coefficient versus bulk viscosity in Fig. 5(b).
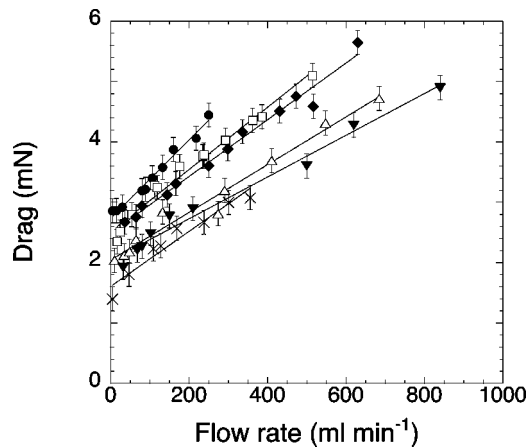
FIG. 6. Drag vs flow rate, for bubble area equal to 12.1 ($\bullet$), 16.0 ($\square$), 20.0 ($\blacklozenge$), 25.7 ($\triangle$), 31.7 ($\blacktriangledown$), and 39.3 mm^2 ($\times$). The straight lines are linear fits of the data. The bulk viscosity is 1.06 mm^2 s^{-1} and the obstacle is a circle of diameter 30 mm.

Figure 5(a) shows that the yield drag is essentially independant of the bulk viscosity. This was expected, because yield drag is only related to the yield properties of the foam, which depend on surface tension and bubble size [29]. The slight decrease with bulk viscosity is due to the slight decrease of the surface tension with the concentration of glycerol: between the solution without gylcerol and the one with 50% glycerol in the mass, the yield drag decreases of $13\pm7\%$, whereas the surface tension decreases of $7\pm1\%$. This is also fully compatible with the slight decrease of the surface tension for pure water-glycerol mixtures (6% in the studied range of concentration [30]).

Figure 5(b) shows that the viscous coefficient increases with the bulk viscosity. The data can be fitted by a power law [inset of Fig. 5(b)], which yields the following dependence of viscous coefficient on bulk viscosity: $m \propto \nu^{0.77\pm0.05}$, the error bar being obtained by the statistical dispersion of the data in the inset of Fig. 5(b).

B. Influence of the bubble area

We now turn to the study of drag versus flow rate and bubble area. All the measurements are done without adding glycerol in the solution, at a constant viscosity of 1.06 mm^2/s. The obstacle is a cylinder of radius 30 mm. We study the six bubble areas indicated in Sec. II C, from 12.1 mm^2 to 39.3 mm^2.

We find again the signature of the viscoelastic properties of the foam (Fig. 6), with a nonzero yield drag and an increase of drag versus flow rate. We perform again a linear fit (3), despite a slight nonaffine variation for 39.3 mm^2, and get the yield drag and the viscous coefficient, plotted versus bubble area in Fig. 7.

Figure 7(a) evidences that the yield drag is a decreasing function of the bubble area. This is coherent with the fact that both quantities used to describe the solid properties of the foam—its shear modulus and yield stress—are also decreasing functions of the bubble size [3,4,31]. Figure 7(b) shows that the viscous coefficient is also a decreasing func-
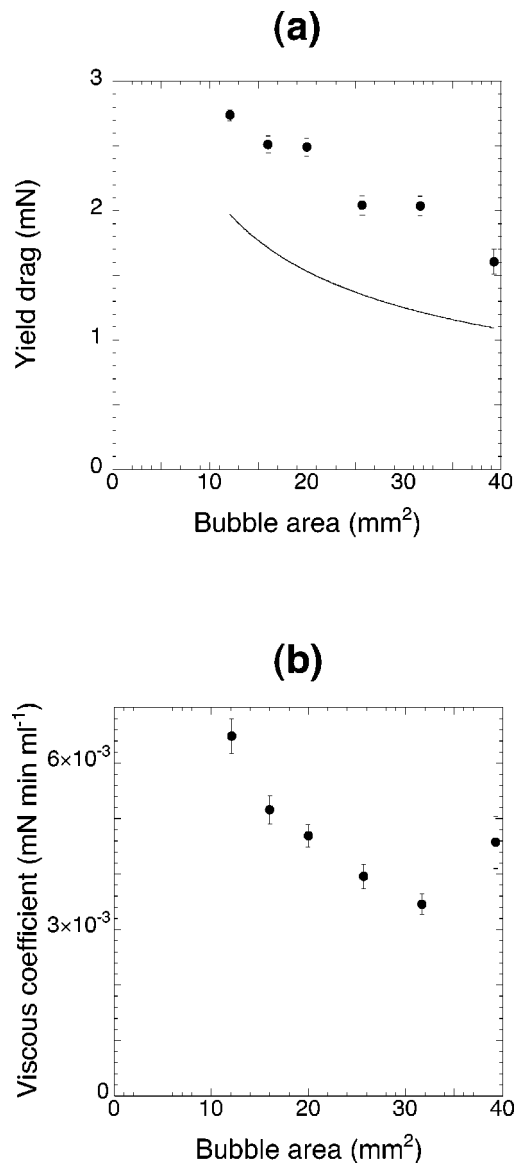

FIG. 7. Results from fits to Fig. 6. (a) Yield drag vs bubble area. The curve is an evaluation of the elastic contribution to the drag: see Sec. IV C. (b) Viscous coefficient vs bubble area.

tion of bubble area, except for the last point. The data will be discussed in more detail in Sec. IV C.

C. Influence of the obstacle geometry

We now study a third control parameter, the obstacle geometry, using the five obstacles described in Sec. II C. As in the previous section, a solution of viscosity of 1.06 mm^2 s^{-1} is used. A bubble area of 16.0 mm^2 was chosen to ensure an optimal trapping of the bubbles in the cogs of the cogwheel. We focus successively on the influence of orientation, size, shape, and boundary conditions of the obstacles.

1. Orientation

Because of their symmetry, the cylinders and cogwheel do not display any orientation effect. We thus focus on the in-
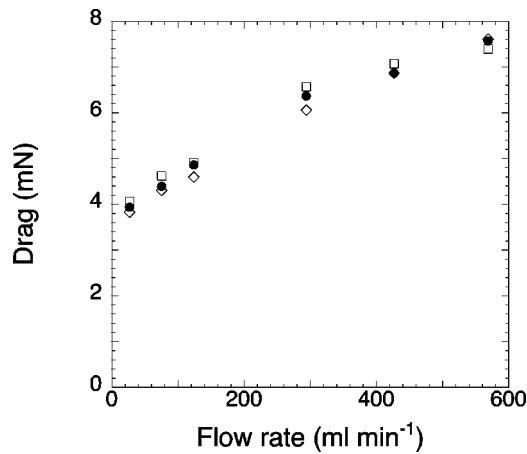
FIG. 8. Drag on the square obstacle vs flow rate, for orientation equal to 0 (●), 22.5 (□), and 45 (◇). The bulk viscosity is 1.06 mm² s⁻¹ and the bubble size is 16 mm².

FIG. 10. Viscous coefficient vs yield drag for the five obstacles, whose photos are sketched near the corresponding data. The straight line is the linear fit passing through zero of the data.

2. Size, shape, and boundary conditions

Measurements of drag versus flow rate for the five different obstacles are displayed in Fig. 9. Here again, all data are well linearly fitted, and as expected, the drag increases with the size of the obstacle. A more quantitative comparison of the obstacles is not straightforward, since not only their size, but also their shape and boundary conditions, vary. To investigate the role of all these parameters, we report the viscous coefficient versus the yield drag for the five obstacles and do a linear fit passing through zero of all the data (Fig. 10). This enables us to compare the respective magnitude of elastic and viscous contribution to the drag and to define an effective drag F_{eff} as the orthogonal projection of the data under linear fit: $F_{eff}=(m+AF_0)/2A$, where $A=(1.81\pm0.08)\times10^{-3}$ min ml⁻¹ is the slope of the linear fitting line. We also define a dimensional drag coefficient, is units of mN mm⁻¹, as the ratio of the effective drag and the transverse length (orthogonal to the flow), in analogy with the dimensionless drag coefficient usually defined in aerodynamics, proportional to the drag and inversely proportional to the cross section and the velocity of the flow [32]. The values of viscous coefficient, yield drag, their ratio, and the dimensional drag coefficient are displayed in Table I, and the values for the dimensional drag coefficient are displayed as histograms in Fig. 11.

IV. DISCUSSION

A. Comparison of our measurements with existing work

To our knowledge, our work is the first to provide systematic measurements of the drag exerted by a flowing foam in a channel around an obstacle. This is to compare to the simulations of Zisis and Mitsoulis [33,34], who computed the drag exerted by a flowing Bingham plastic past a cylinder similar in geometry to our circle, for different values of obstacle diameters. A Bingham plastic is characterized by its yield stress τ_y and its plastic viscosity μ, and it follows the

fluence of the orientation relative to the flow direction of the square on the drag measurements.

We have checked that for the square obstacle, any given orientation is stable. More precisely, orientation drifts under 90 min are always less than 5° (data not shown), although it is a much longer duration than what is required for the measurements. We have studied the variation of drag versus flow rate for three orientations of the square between a side and the flow direction: 0°, 22.5°, and 45°. Figure 8 shows that the drag does not depend significantly on the orientation: henceforth, drag measurements on the obstacle will be averaged over these three orientations.

Contrary to the circle, the airfoil only possesses two stable orientations when its plane of symmetry is parallel to the flow direction. The more stable configuration is obtained when foam flows from the rounded leading edge to the sharp trailing edge, which is the usual configuration in aerodynamics.
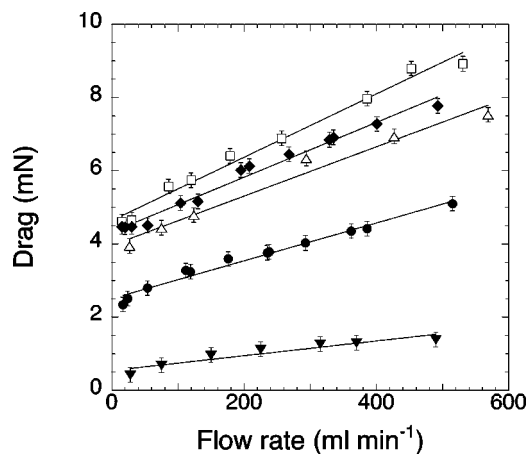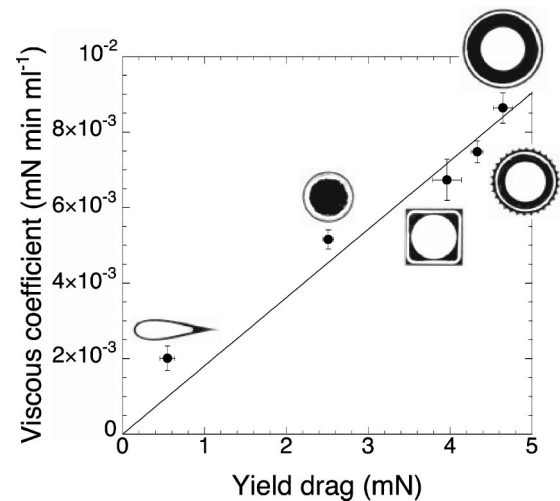

FIG. 9. Drag vs flow rate, for the cylinder of diameter 30.0 mm (●) and 48.0 mm (□), the cogwheel (◆), the square (△) and the airfoil (▼). The straight lines are linear fits of the data. The bulk viscosity is 1.06 mm² s⁻¹ and the bubble area is 16 mm².

TABLE I. Yield drag F_0, viscous coefficient m, ratio m/F_0, and dimensional drag coefficient C_x for each obstacle. The star symbol recalls that the drag coefficient for the square depends on its orientation: the value of this coefficient expressed in mN mm^{-1} is 0.113±0.010 for an orientation angle of 0°, 0.087±0.010 for an angle of 22.5°, and 0.080±0.005 for an angle of 45°.

Obstacle	Cylinder ⌀ 30 mm	Cylinder ⌀ 48 mm	Cogwheel	Square	Airfoil
F_0 (mN)	2.5±0.1	4.6±0.1	4.3±0.1	4.0±0.2	0.5±0.1
m (mN min l^{-1})	5.2±0.3	8.6±0.4	7.5±0.3	6.7±0.5	2.0±0.3
m/F_0 (min l^{-1})	2.1±0.2	1.9±0.1	1.7±0.1	1.7±0.2	3.7±1.2
C_x (mN mm^{-1})	0.089±0.006	0.098±0.006	0.097±0.005	*	0.066±0.013

constitutive equation $\tau = \tau_y + \mu\dot{\gamma}$ for $|\tau| > \tau_y$ and $\dot{\gamma} = 0$ for $|\tau| < \tau_y$, where τ is the shear stress and $\dot{\gamma}$ the applied strain. To summarize, Zisis and Mitsoulis show that the drag exerted by a flowing Bingham plastic around a cylinder strongly depends on the Bingham number Bn$=2R\tau_y/\mu V$ comparing elastic and viscous contributions: at a given Bingham number of order unity, there is a crossover between a Newtonian-like behavior of the drag (for Bn$\ll 1$) given by formula (2) and an elastic-like (for Bn$\gg 1$) where drag does not significantly depend on the velocity and is roughly proportional to the cylinder diameter. Though the validity of modeling foam as a Bingham plastic is an open debate, this work provides an interesting comparison to our experimental measurements, for which we now evaluate the order of magnitude of the Bingham number. The yield stress for a foam is of order [29] $0.5\gamma/a$, with $\gamma = 26.1$ mN m^{-1} the surface tension and $a \approx \sqrt{16/(3^{3/2}/2)} \approx 2.5$ mm the typical length of a bubble edge (we recall that the bubble area is 16.0 mm^2 in the considered experiments and compute a for a hexagonal bubble), so $\tau_y \approx 5$ Pa (to be rigorous, this overestimates the yield stress for a wet foam). Furthermore, we can deduce from the value of the viscous coefficient [$m = 5 \times 10^{-6}$ N min ml^{-1} after Fig. 7(b)] a rough value of the plastic viscosity of the foam: dimensional analysis yields $\mu \approx mS/R$ where S is the cross section of the foam, so the Bingham number is written Bn$\approx 2R^2\tau_y/mQ$. The typical value of flow rate in our experiments is 10^2 ml min^{-1}; hence, the typical Bingham number equals Bn$\approx (2 \times 0.015^2 \times 6)/(5 \times 10^{-6} \times 10^2) \approx 5$. Though this is a very rough evaluation, it tends to show that in our

range of flow rates, the Bingham number remains of order unity, and hence both elastic and fluid properties of the foam are involved in the interaction with the obstacle to create the drag. This corroborates the measurements of drag in Fig. 9 for which elastic and plastic contributions are of the same order of magnitude.

B. Influence of the bulk viscosity

Our measurements of drag versus viscosity ν and flow rate Q yield the following scaling:

$$F(Q,\nu) = F_0 + \text{const} \times \nu^{0.77\pm0.05}Q \qquad (4)$$

(see Sec. III A). To our knowledge, this is the first time that such a scaling is proposed to quantify the dynamical regime of flowing foams. Up to now, the dynamic regime of flowing foam has been mainly investigated through the study of pressure drop of foam confined in capillaries (see Ref. [35] and references therein), to model the behavior of foams in porous media [36,37]. Since the seminal work of Bretherton [38], who studied the friction between an infinitely long bubble and a solid wall, all these studies emphasize the role of the capillary number Ca$=\eta V/\gamma$, where η is the dynamic bulk viscosity, γ its surface tension, and V the velocity of the flowing foam. In the frame of our study, the capillary number is proportional to the product νQ. It appears from our scaling (4) that such a number is not sufficient to describe the dynamic regime of a flowing foam, because the exponents for viscosity and flow rate differ significantly, and pressure drop measurements confirm this observation [43]. Since the velocity-dependent part of the drag is related to friction of slipping bubbles along the obstacle, Bretherton's theory is therefore not sufficient to explain our measurements: additional physical ingredients are involved, like detailed bubble shape and interfacial rheology (surface elasticity and viscosity). This has not been investigated yet. Discrepancies from Bretherton's theory have already been widely pointed out and studied for bubbles and foams in capillaries (see Ref. [39] for a review), but they still considered the capillary number as the essential dimensionless parameter.

Let us notice that the scaling (4) is a consequence of the chosen fit (3). We are aware that some rheological studies [3,4,6] show that storage and loss moduli of foams happen to depend on the applied shear. This would lead to a behavior like $F = F_0 + mQ^\alpha$, the exponent α accounting either for shear thinning ($\alpha < 1$) or shear thickening ($\alpha > 1$). If such effects exist in our system, they are small enough to yield results consistent with $\alpha = 1$ within our experimental accuracy. We
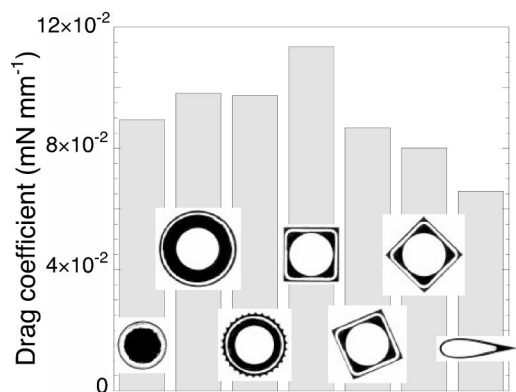

FIG. 11. Dimensional drag coefficient for all obstacles. Since the drag exerted on the square does not significantly depend on its orientation whereas the cross length does, we give the drag coefficient for the three studied orientations of the square.

will thus neglect shear thinning or shear thickening in our further discussion.

C. Influence of the bubble area

1. Yield drag

The yield drag has two contributions: an elastic one arising from the elastic stresses in the network of bubbles and another one arising from the anisotropic pressure distribution in the bubbles surrounding the obstacle, as already shown in preliminary simulations of our experiments [40].

As mentioned in Sec. II C, the depth of the bubbles adjusts to pressure variations. At constant bubble volume, there is therefore a relation between bubble area and pressure that we can use to evaluate the order of magnitude of the pressure contribution to the yield drag. To establish this relation, we assume that each bubble has the same volume V_0, which is reasonable in our experiments. As a crude model, we treat bubbles as cylinders of height h and of horizontal area A; hence, $V_0 = A_0 h_0 = Ah$, where A_0 and $h_0 = 3.5$ mm refer to mean values. We then assume that the pressure P inside the bubbles equilibrates with the pressure in the bulk solution in contact. At vanishing flow rate, this pressure is hydrostatic; hence, we write $P - P_0 = \rho g h = \rho g A_0 h_0 / A$, where P_0 is a constant reference pressure and $\rho = 1.0 \times 10^3$ kg/m^3 is the volumetric mass of the solution. The pressure resultant on the obstacle is then written $\mathbf{F}_P = -\iint P d\mathbf{S}$, the integral being taken on the contact surface between the obstacle and bubbles. Since P_0 is constant, $\mathbf{F}_P = -\rho g A_0 h_0 d\mathbf{S}/A$ and $d\mathbf{S} = h d\ell \mathbf{n}$, where $d\ell$ is the length element on the boundary of the obstacle and $\mathbf{n}$ the normal vector. Since $h = A_0 h_0 / A$, one obtains

$$\mathbf{F}_P = -\rho g A_0^2 h_0^2 \oint \frac{d\ell \mathbf{n}}{A^2}. \qquad (5)$$

This formula links the pressure contribution to yield drag to the bubble area field.

We illustrate this measurement of pressure on one example (Fig. 12). The bubble area field clearly shows the influence of the obstacle: bubbles are compressed upstream and relax downstream, which qualitatively shows that the pressure resultant acts in the same sense as elastic stress. Computing formula (5) over the dashed contour in Fig. 12, which is the closest contour to the obstacle where bubble area is properly evaluable, yields an order of magnitude of 0.7 mN for F_P, which is about 30% of the yield drag [2.5 mN for the studied example; see Fig. 7(a)]. The calculation of pressure for various bubble areas, as well as for higher flow rates and other obstacles, is still in progress, but the variation depicted in Fig. 12 does not vary qualitatively and the pressure contribution to yield drag is not negligible.

Another difficulty arises from the variation of fluid fraction with bubble area. In our setup, the monolayer of bubbles is in contact with a reservoir of water, and the amount of water in the Plateau borders and films between bubbles is freely chosen by the system. Therefore, the mean fluid fraction should vary with bubble area; detailed measurements of this quantity are in progress (first rough estimate: about 9%).
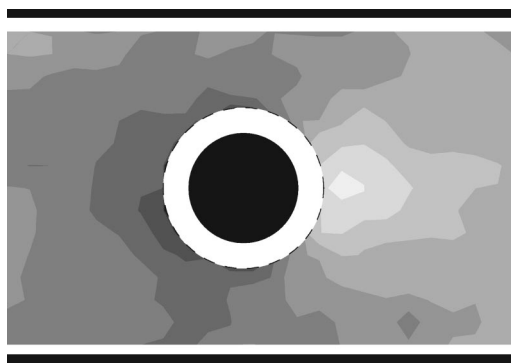

FIG. 12. Bubble area field around the circle of diameter 30 mm. The observed zone is the same as Fig. 2. The solution viscosity is 1.06 mm^2 s^{-1}, and the mean bubble area is $A_0 = 16.0$ mm^2. The flow rate 24 ml min^{-1} was chosen such that the velocity-dependent contribution to the drag is negligible (see Fig. 6). Black zones represent the obstacle and the channel walls and white zones the regions where the bubble area is not measurable precisely. The darker the color, the lower the bubble area hence the higher the pressure. The area variation is significant, with a maximum relative variation of 18%. The pressure is maximal at the leading side of the circle and minimal at its trailing side (maximal variation: 70 Pa).

Furthermore, local effects such as dilatancy [41] could increase the fluid fraction near the obstacle, because of the shear experienced by the foam in this zone. This complicates the interpretation of the evolution of yield drag with bubble area, since many studies have shown that rheological properties of foams and emulsions depend on fluid fraction [3,4,6]. However, we can check that the order of magnitude of our measured yield drag agrees qualitatively with the known value of the yield stress, of order [29] $0.5\gamma/a$. Hence, the order of magnitude of the elastic contribution to the yield drag is $F_{\text{el}} \approx \pi R h_0 \gamma / a$. For an hexagonal bubble, $a = \sqrt{2A/3^{3/2}} = 0.62\sqrt{A}$; hence, $F_{\text{el}} \approx 5 R h_0 \gamma / \sqrt{A}$ and, numerically, $F_{\text{el}} \approx 7/\sqrt{A}$, with mN and mm^2 as units for the force and for the area. This elastic drag is plotted in Fig. 7; though it is a very rough evaluation, we check that it is of the same order of magnitude as the yield drag, but that it is not high enough to fit the experimental results: this is again a signature of the significance of the pressure contribution.

2. Viscous coefficient

We now propose a qualitative argument to explain why the viscous coefficient decreases with the bubble area, based on the dissipation model of Cantat and co-workers [35]. These authors state that dissipation in flowing foam is localized in the Plateau borders between bubbles and walls. Hence, the viscous coefficient should increase with the number of bubbles surrounding the obstacle and therefore should decrease with the bubble area, which is actually seen in Fig. 7(b). Note that this model does not capture the increase observed for the bubble area of 39.3 mm^2, but as seen in Fig. 6, the drag does not depend affinely on the flow rate for this area, and hence our linear fit is not relevant. As an additional remark, friction in the foam should strongly depend on the boundary conditions at the interfaces between films and

bubbles, and hence the viscous coefficient probably changes with the surface rheology. It would thus be interesting to investigate the influence of the surfactant used on the drag measurements.

D. Influence of the obstacle geometry

1. Orientation

We have shown (Fig. 8) that the drag exerted on the square obstacle does not significantly depend on its orientation. The same result holds in low Reynolds hydrodynamics, merely owing to the linearity of the Stokes equation and to the high symmetry of the square [42]. On the other hand, the drag does depend on the orientation at high Reynolds number [32]. We thus think this result provides a good test to validate possible constitutive equations for foams; it tends to prove the relevance of linear models, at least in the studied range of control parameters.

2. Size, shape, and boundary conditions

We have chosen to compare the various obstacles through an effective drag and a ratio between the viscous coefficient and the yield drag. We think this is relevant since this way of comparison involves both the elastic and the viscous contribution to the drag, which have comparable weight in the studied range of flow rate (Fig. 9). Furthermore, this provides a way to compare obstacles of different shapes.

Figure 11 shows that the dimensional drag coefficient does not vary much with the obstacle, except for the airfoil. Though the cross length is not the unique characteristic length of the obstacles, this shows that the drag is roughly proportional to the size of the obstacle. This is not an obvious result: considering the flow of a Newtonian fluid around a cylinder in the same geometry as ours, and defining like before a drag coefficient as the ratio between the drag (2) and the radius of the cylinder, it can be shown that this drag coefficient would increase significantly with the radius. The complete formula (2), not shown for the sake of simplicity (see Ref. [27]), yields a drag coefficient 2.6 times higher for a cylinder of diameter 48 mm than for the one of diameter 30 mm, whereas the values of Table I show that the drag coefficients for these two cylinders are comparable in our experiments. This proves again the significance of elastic effects in our case and agrees qualitatively with the results of Mitsoulis [34] who showed that for a Bingham plastic, the effect of channel walls remains weak, even when the diameter of the cylinder equals the half of the channel width, as far as elastic effects are dominant.

The ratio between viscous coefficient and yield drag, whose values are tabulated in Table I, does not change significantly between the cylinders, the cogwheel, and the square, whereas it increases much for the airfoil. This is clearly a signature of shape: one intuitively expects elastic effects to act on the cross section orthogonal to the flow to pull the obstacle streamwise, whereas the viscous contribution to the drag arises from the friction in the lubrication films between the obstacle and bubbles slipping along it. Hence, one expects the viscous contribution to increase with the cross section parallel to the flow. This explains why the viscous coefficient/yield drag ratio is higher for the airfoil, owing to the great difference between the two considered sections for this profile. Furthermore, the decrease of the drag coefficient for the airfoil, as well as the variation of this coefficient with the orientation of the square, shows that the shape of the obstacles influences the results through streamlining: for a given size, drag is reduced on an obstacle whose shape is well adapted to the flow, like in aerodynamics.

The values displayed in Table I show that the boundary conditions do not affect much the drag: the dimensional drag coefficient is close to those for the two cylinders, whereas the ratio between viscous coefficient and yield drag is slightly lower. Actually, the cogwheel and trapped bubbles form a closed system during the experiment: no rearrangement of the trapped bubbles occurs after all the cogs have been filled with bubbles. So this system behaves as an effective obstacle, but with an external boundary constituted of bubble edges, instead of a solid boundary. This could explain the slight decrease of the viscous coefficient/yield drag ratio: at low velocity, the foam feels the presence of the effective obstacle, but at high velocity, the friction between this effective obstacle and the surrounding flowing bubbles is lower than the friction between a solid obstacle and its neighboring flowing bubbles. To be more quantitative, it would be interesting to study the influence of interfacial rheology on this friction. Anyway, the measurements show that the influence of boundary conditions is not dramatic, probably because it does not change much the features of the flow beyond the first layer of bubbles.

V. CONCLUSIONS

This work provides the first detailed and systematic measurements of the force exerted by a 2D flowing foam on an obstacle as a function of various control parameters: flow rate, bulk viscosity, bubble volume, obstacle orientation, and size, shape, and boundary conditions. All the data show two contributions to the drag: a yield drag at vanishing flow rate and a flow rate-dependent contribution. We have shown that the yield drag is independent of the bulk viscosity, decreases with bubble volume, and linearly increases with the obstacle size. Moreover, both elastic stresses and pressure contribute significantly to the yield drag. Fitting the flow rate-dependant contribution by a linear law, we have shown that the slope (or viscous coefficient) increases with the bulk viscosity as a power law with an exponent around 3/4; moreover, the viscous coefficient globally decreases with the bubble volume and linearly increases with the obstacle size. Furthermore, we have studied the influence of the obstacle shape and showed the existence of streamlining effects in foams, and we pointed out that the effect of boundary conditions on the obstacle is not striking.

This work opens many perspectives. Other control parameters remain to be studied, like bubble area polydispersity and rheological properties of the surfactants. The effects of those parameters on the drag could help to study their influence on foam rheology. Pressure drop measurements, allowing one to study dissipation in foams [35], are in progress

[43]. Now, a local analysis of the stresses, deformations [44], and velocity fields is required to provide a more detailed comprehension of the foam rheology. Such a study is also in progress. The comparison between this local analysis and the global properties of the foam, such as our drag measurements, could provide a way to propose and test constitutive equations for the mechanics of foams.

ACKNOWLEDGMENTS

APPENDIX: DERIVATION OF FORMULA (1)

We consider a fiber of vertical length L that experiences a horizontal force F (Fig. 13). All lengths are adimensionalized by $\sqrt{IE/2F}$, where $I=\pi D^4/64$ is the inertia moment (D being the fiber diameter) and E the Young modulus. The position along the fiber is expressed as a function of the angle α. Therefore, the position of the extremity of the fiber is written in the general case [26],

$$L = 2\sqrt{\sin \alpha_0},$$

$$X = \int_0^{\alpha_0} \frac{\sin \alpha}{\sqrt{\sin \alpha_0 - \sin \alpha}} d\alpha \Rightarrow X$$

$$= \int_0^{\arcsin L^2/4} \frac{\sin \alpha}{\sqrt{L^2/4 - \sin \alpha}} d\alpha.$$

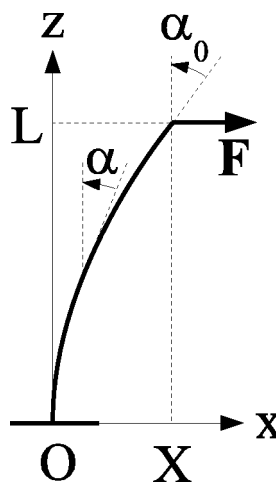This yields an implicit expression between the force and de-

FIG. 13. Notations for the calculation of formula (1).

flection involving elliptic functions, which is not easy to evaluate.

The fiber can experience large deflections (up to 12 mm for a length of 34.8 mm), so we need a more accurate expression than the linearized one: $X=L^3/6$. To do that, we develop the previous expression in power series of L, which yields $X=L^3/6+L^7/280+L^{11}/7392+O(L^{15})$. Going back to dimensionalised lengths and inverting the series yields the formula (1) linking the force and deflection.

At the maximal deflection, the ratio X/L reaches a value of 0.345. At such a ratio, formula (1) gives a precision of 0.3% over the force, while the linearized formula $F=3\pi ED^4X/64L^3$ yields an error of 9%.

[1] R. G. Larson, *The Structure and Rheology of Complex Fluids* (Oxford University Press, New York, 1999).

[2] D. Weaire and S. Hutzler, *The Physics of Foams* (Oxford University Press, Oxford, 1999).

[3] T. G. Mason, J. Bibette, and D. A. Weitz, Phys. Rev. Lett. **75**, 2051 (1995).

[4] T. G. Mason, J. Bibette, and D. A. Weitz, J. Colloid Interface Sci. **179**, 439 (1996).

[5] S. Cohen-Addad, H. Hoballah, and R. Höhler, Phys. Rev. E **57**, 6897 (1998).

[6] A. Saint-Jalmes and D. J. Durian, J. Rheol. **43**, 1411 (1999).

[7] D. A. Reinelt and A. Kraynik, J. Rheol. **44**, 453 (2000).

[8] P. Sollich, F. Lequeux, P. Hébraud, and M. E. Cates, Phys. Rev. Lett. **78**, 2020 (1997).

[9] D. J. Durian, Phys. Rev. Lett. **75**, 4780 (1995).

[10] M. E. Cates and P. Sollich, J. Rheol. **48**, 193 (2004).

[11] R. Höhler, S. Cohen-Addad, and V. Labiausse, J. Rheol. **48**, 679 (2004).

[12] C. Monnereau and M. Vignes-Adler, in *Foams and Emulsions* edited by J. F. Sadoc and N. Rivier, Vol. 354 of *NATO Advanced Study Institute, Series E: Applied Sciences* (Kluwer, Dordrecht, 1999), p. 359.

[13] B. Prause, J. A. Glazier, S. Gravina, and C. Montemagno, J. Phys.: Condens. Matter **7**, L511 (1995).

[14] J. Lambert, I. Cantat, R. Delannay, G. Le Caër, A. Renault, S. Ruellan, F. Graner, S. Jurine, P. Cloetens, and J. A. Glazier, proceedings of Eufoam 2004, Colloids Surf., A (to be published).

[15] S. A. Koehler, S. Hilgenfeldt, and H. A. Stone, Europhys. Lett. **54**, 335 (2001).

[16] M. Lösche, E. Sackmann, and H. Möhwald, Ber. Bunsenges. Phys. Chem. **87**, 2506 (1983).

[17] S. Courty, B. Dollet, F. Elias, P. Heinig, and F. Graner, Europhys. Lett. **64**, 709 (2003).

[18] A. Abd el Kader and J. C. Earnshaw, Phys. Rev. Lett. **82**, 2610 (1999).

[19] E. Pratt and M. Dennin, Phys. Rev. E **67**, 051402 (2003).

[20] C. S. Smith, in *Metal Interfaces* (American Society for Metals, Cleveland, OH, 1952), p. 65.

[21] G. Debrégeas, H. Tabuteau, and J.-M. di Meglio, Phys. Rev.

Lett. **87**, 178305 (2001).

[22] M. Asipauskas, M. Aubouy, J. A. Glazier, F. Graner, and Y. Jiang, Granular Matter **5**, 71 (2003).

[23] M. F. Vaz and M. A. Fortes, J. Phys.: Condens. Matter **9**, 8921 (1997).

[24] É. Janiaud and F. Graner, e-print cond-mat/0306590, J. Fluid Mech (to be published).

[25] S. J. Cox, M. D. Alonso, S. Hutzler, and D. Weaire, in *Proceedings of the 3rd Euroconference on Foams, Emulsions and their Applications*, edited by P. L. J. Zitha, J. Banhart, and G. L. M. M. Verbist, (Verl. MIT, Bremen, 2000).

[26] L. D. Landau and E. M. Lifshitz, *Theory of Elasticity* 3rd ed. (Reed, Oxford, 1986).

[27] O. H. Faxén, Proc. R. Swed. Acad. Eng. Sci. **187**, 1 (1946).

[28] S. J. Cox, D. Weaire, and M. F. Vaz, Eur. Phys. J. E **7**, 311 (2002).

[29] H. M. Princen, J. Colloid Interface Sci. **91**, 160 (1983).

[30] D. R. Lide, *CRC Handbook of Chemistry and Physics*, 84th ed. (CRC Press, Boca Raton, 2003).

[31] H. M. Princen, J. Colloid Interface Sci. **105**, 150 (1985).

[32] R. Comolet, *Mécanique Expérimentale des Fluides* (Masson, Paris, 1976), Vol. II.

[33] T. Zisis and E. Mitsoulis, J. Non-Newtonian Fluid Mech. **105**, 1 (2002).

[34] E. Mitsoulis, Chem. Eng. Sci. **59**, 789 (2004).

[35] I. Cantat, N. Kern, and R. Delannay, Europhys. Lett. **65**, 726 (2004).

[36] P. L. J. Zitha, Transp. Porous Media **52**, 1 (2003).

[37] Q. Xu and W. R. Rossen, Colloids Surf., A (to be published).

[38] F. B. Bretherton, J. Fluid Mech. **10**, 166 (1961).

[39] K. G. Kornev, A. V. Neimark, and A. N. Rozhkov, Adv. Colloid Interface Sci. **82**, 127 (1999).

[40] S. J. Cox (private communication).

[41] D. Weaire and S. Hutzler, Philos. Mag. **83**, 2747 (2003).

[42] É. Guyon, J.-P. Hulin, and L. Petit, *Hydrodynamique Physique* EDP Sciences/CNRS Éditions, (Paris, 2001).

[43] B. Dollet, F. Elias, C. Quilliet, A. Huillier, M. Aubouy, and F. Graner, in *Proceedings of the 5rd European Conference on Foams, Emulsions and Applications*, Colloids Surf., A (to be published).

[44] M. Aubouy, Y. Jiang, J. A. Glazier, and F. Graner, Granular Matter **5**, 67 (2003).